Speed and delivered power in waves — Predictions with CFD simulations at full scale

Downloaded from: https://research.chalmers.se, 2026-04-04 12:10 UTC

Citation for the original published paper (version of record):
Orych, M., Östberg, M., Kjellberg, M. et al (2023). Speed and delivered power in waves — Predictions with CFD simulations at full scale. Ocean Engineering, 285. http://dx.doi.org/10.1016/j.oceaneng.2023.115289

N.B. When citing this work, cite the original published paper.

research.chalmers.se offers the possibility of retrieving research publications produced at Chalmers University of Technology. It covers all kind of research output: articles, dissertations, conference papers, reports etc. since 2004. research.chalmers.se is administrated and maintained by Chalmers Library

(article starts on next page)

Ocean Engineering 285 (2023) 115289

Contents lists available at ScienceDirect

Ocean Engineering

journal homepage: www.elsevier.com/locate/oceaneng

Speed and delivered power in waves — Predictions with CFD simulations at full scale

Michal Orych [a,d,*], Magnus Östberg [d], Martin Kjellberg [b], Sofia Werner [b], Lars Larsson [a,c]

[a] Department of Mechanics and Maritime Sciences, Chalmers University of Technology, Gothenburg, Sweden
[b] RISE Research Institutes of Sweden/SSPA Sweden AB, Gothenburg, Sweden
[c] International School of Yacht Design – ISYD AB, Sweden
[d] FLOWTECH International AB, Gothenburg, Sweden

ARTICLE INFO

Keywords:
Seakeeping
EEDI
Weather factor
Delivered power
Speed loss
Full-scale
Self-propulsion
validation
CFD

ABSTRACT

An efficient numerical method is proposed to estimate delivered power and speed loss for a ship in wind and waves. The added resistance in waves, obtained with an unsteady potential flow panel method, is added to the calm water resistance from a steady-state potential flow/RANS method coupled with a body force propeller model for self-propulsion. A comparison of numerical and experimental results is made for added resistance, calm water resistance and delivered power. A good agreement is obtained. As a practical application, the approach is used to calculate the weather factor, f_w, of the Energy Efficiency Design Index (EEDI). The calculated weather factor is consistent with the values derived from full-scale measurements included in a database of similar ships.

1. Introduction

Computational Fluid Dynamics (CFD) is presently an accepted tool for predicting calm water resistance and powering at model scale. The development of this area is well covered by the International Workshops on Numerical Ship Hydrodynamics, see Larsson et al. (2014) and Hino et al. (2021). However, to obtain full-scale data, the results have to be extrapolated. More recently, the interest has shifted towards direct full-scale predictions, and the currently most comprehensive validation exercise is performed within the Joint Research Project, "Development of Industry-Recognised Benchmark for Ship Energy Efficiency Solutions", JoRes (2023). In a recent paper, the authors also demonstrated the feasibility of this approach, Orych et al. (2021).

However, ship designers place greater emphasis on real-world conditions, which include environmental factors like wind and waves. Historically, seakeeping studies have primarily relied on experimental testing in towing tanks or model basins, but numerical predictions are becoming more and more popular. They can be used, for example, to estimate the weather factor (ITTC, 2021b), which is a part of the Energy Efficiency Ship Index (EEDI) (IMO, 2018), and they are accepted for computing the calm water reference speed for the Energy Efficiency Existing Ship Index (EEXI) (IMO, 2022).

A hierarchy of numerical methods for seakeeping performance is presented in Fig. 1, showing their level of approximation versus computational effort. At the far end of the x-axis is the simple frequency domain strip method, which is extremely rapid on today's computers. The next method is an extension to non-linear strip theory in the time domain. Then there are two 3D boundary element (BEM) methods, the first one being linear and the second one non-linear. The unsteady Reynolds-Averaged Navier–Stokes (RANS) method is next. It introduces a more physically accurate representation of reality but requires much more computational effort than the non-linear BEM. At the most exact end of the graph, there is Large Eddy Simulation, LES, which is still too expensive to be applied in the industry, and Direct Numerical Simulation, DNS, entirely out of reach for practical applications.

At present, the best compromise between accuracy and computational demands are the RANS and non-linear BEM methods. While the former is more popular, there is a rather severe limitation in the number of computations that can be carried out in a reasonable time. A hybrid method was proposed by Kim et al. (2017), who used linear 2-D and 3-D potential flow methods, as well as unsteady RANS, to evaluate added resistance in waves, but the calm water resistance and speed loss in waves were estimated with simplified methods. Saettone (2020) used an unsteady potential flow 6DOF method combined with a double-model RANS code coupled with a propeller analysis tool based on a boundary-element method. His work indicates that this approach could determine the mean propulsive power in moderate waves with relatively good accuracy.

* Corresponding author at: Department of Mechanics and Maritime Sciences, Chalmers University of Technology, Gothenburg, Sweden.
E-mail address: michal@flowtech.se (M. Orych).

https://doi.org/10.1016/j.oceaneng.2023.115289
Received 15 March 2023; Received in revised form 14 June 2023; Accepted 29 June 2023
Available online 11 July 2023
0029-8018/© 2023 The Author(s). Published by Elsevier Ltd. This is an open access article under the CC BY license (http://creativecommons.org/licenses/by/4.0/).

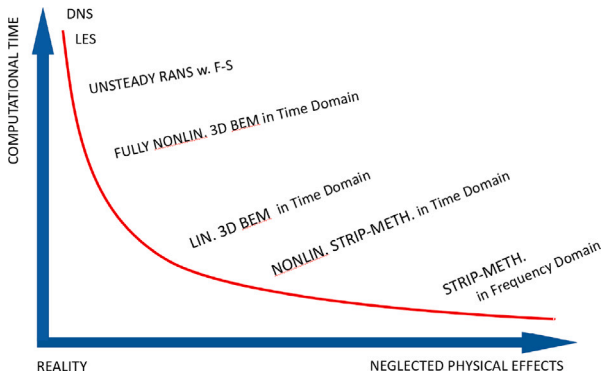

Fig. 1. Computational methods for seakeeping.

Nomenclature

ω	Specific turbulence dissipation rate
C_F	Frictional resistance coefficient
C_P	Pressure resistance coefficient
C_T	Total resistance coefficient
C_{AW}	Added resistance in waves coefficient
f_w	Weather factor
k	Turbulent kinetic energy
k_S	Equivalent sand grain roughness height
n_g	Number of grid cells
P_D	Delivered power
U_G	Grid uncertainty

Even though it is possible to combine hydro- and aerodynamic simulations in one computation as presented by Zhang and Kim (2018), it is not practical to combine it with seakeeping. It is a common practice to consider wind resistance in self-propulsion simulations as an external resistance component. This can be estimated through wind tunnel testing, CFD methods or empirical formulations, ITTC (2021b).

In this paper, we propose a similar hybrid BEM/RANS method for predicting the powering performance, including speed loss, of full-scale ships in irregular waves. The method is based on a newly developed, fully nonlinear, unsteady potential flow solver for free surface flows with floating bodies, subject to 6DOF, see Coslovich et al. (2021). This gives the added resistance in waves, which is combined with a potential flow for calm water wave resistance and a double-model steady-state RANS solver for self-propulsion at full scale. More than an order of magnitude is gained in computational time compared to unsteady RANS, and the accuracy is at the same level. The method should be of interest both in vessel design and in connection with current and future regulations, such as the EEDI. Note that the scope is limited to normal operating conditions and does not include severe survival modes.

2. Numerical method

The software used in this project is SHIPFLOW, developed over a long period of time at Chalmers University of Technology and FLOWTECH. It includes several modules and solvers. The calm water wave resistance, including sinkage and trim, is computed using the potential flow solver XPAN, (Janson, 1997), and the steady-state RANS solver XCHAP is used to simulate self-propulsion at full scale, Korkmaz (2015). Added resistance is obtained using the newly developed seakeeping module MOTIONS (Coslovich et al., 2021). Results from all the solvers can be combined in a chain of simulations to provide necessary resistance components for self-propulsion simulations in waves.

2.1. Added resistance in waves

MOTIONS is based on a fully nonlinear unsteady potential flow solver for free surface flows with floating bodies subject to 6DOF. It has an internal automatic mesh engine for rigid bodies and the free surface, as well as support for importing externally generated meshes of rigid bodies or environment boundaries. The rigid body meshes are initially refined close to the free surface and in regions with large curvature and, after that, kept the same throughout the computation.

In each time step, the free surface mesh is initialized with a coarse mesh. The free surface panels completely inside a rigid body are then cut away, and panels partially inside a rigid body are split into four panels. This is done a specified number of times recursively. Subsequently, the free surface panel nodes closest to the rigid body are snapped the rigid body. Additionally, the free surface mesh is refined in regions with large free surface curvature, see Fig. 2.

The free surface is traced by markers using a mixed Eulerian–Lagrangian approach. In the Eulerian step, the velocity potential and velocity of each marker are computed with a boundary element method (BEM). In the Lagrangian step, the free surface boundary conditions are integrated in time, and the marker's position and velocity potential are updated.

Once the Lagrangian step is finished, a new free surface mesh is generated by interpolating the surface elevation from the marker's updated positions. In addition, the boundary conditions for the next Eulerian step are obtained by interpolating the velocity potential of the markers. The interpolations on the free surface are done with thin-plate splines, Duchon (1976).

The hull body motions are calculated by summing up the pressure forces on the hull panels and integrating the corresponding rigid body acceleration in time. The total pressure on the hull is given by Bernoulli's equation, and for robustness reasons, an acceleration potential is used to obtain the time derivative of the velocity potential. A 4th-order Adams–Bashforth–Moulton predictor–corrector method is utilized for time integration.

Several measures have been taken to lower the computational time. For instance, a nonlinear decomposition of the solution into an undisturbed incident wave field and a disturbance field due to the presence of the hull, Ducrozet et al. (2014). This ensures that incident waves far from the hull do not have to be resolved by the BEM and thereby larger panels can be used away from the hull without affecting the quality of the incident wave field, which is described analytically by 5th-order Stokes wave theory. Another example is the use of a modified Barnes–Hut algorithm, where panels are grouped together into nodes based on the distance to the point where their influence is to be computed, Barnes and Hut (1986).

The code has an automatic way to detect risks for wave breaking and applies additional pressure in such regions of the free surface to mitigate local wave breaking, Mola et al. (2017). Additionally to avoid wave reflections from the domain boundaries a damping zone is introduced. A forcing term that eliminates the disturbance, i.e. the difference between the undisturbed incident waves and the total computed wave height, is applied close to the outer boundaries, Kjellberg et al. (2022).

2.2. Calm water wave resistance

XPAN is a nonlinear Rankine source panel method, Janson (1997). It uses higher-order panels and singularity distributions. Nonlinear boundary conditions are used for the free surface. Dynamic sinkage and trim are computed during the iterative procedure for the nonlinear free surface boundary condition. During each iteration, the ship is repositioned and the panelization of the hull and free surface is regenerated. An illustration of the hull and free surface panelization is shown in Fig. 3. The resulting heave and pitch are used to position the hull, and the wave resistance is added in the RANS simulations in a one-way coupling. The viscous results do not affect the trim, sinkage and wave resistance.

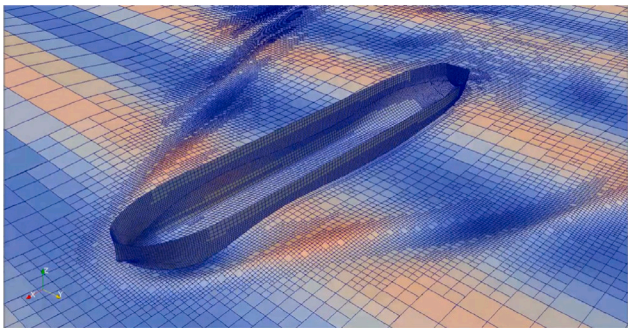

Fig. 2. An example of an adaptive mesh for the free surface.

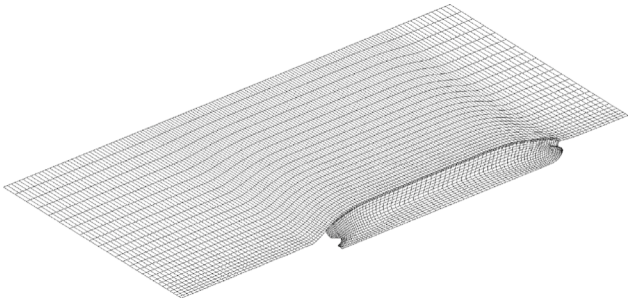

Fig. 3. Free surface and hull meshes used in XPAN simulations.

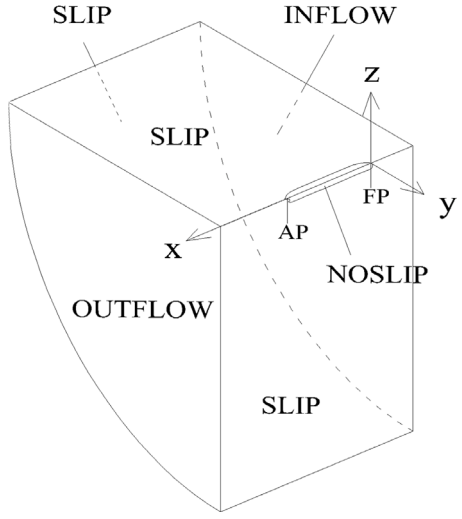

Fig. 4. Illustration of the computational domain and boundary conditions for RANS simulations.

2.3. Calm water self propulsion

XCHAP solves the steady, incompressible RANS equations using a finite volume method. The explicit algebraic stress turbulence model, EASM, Deng et al. (2005), is used in the present paper. No wall functions are used, and the equations are integrated down to the wall. The equations are discretized using the Roe scheme, Roe (1981), for the convection, while a central scheme is used for the diffusive fluxes. An explicit flux correction is applied to achieve second-order accuracy, Dick and Linden (1992), Chakravarthy and Osher (1985).

The hull roughness effect is modeled by a modification of the boundary conditions for the specific dissipation of the turbulent kinetic energy, ω and the turbulent kinetic energy, k, Orych et al. (2022).

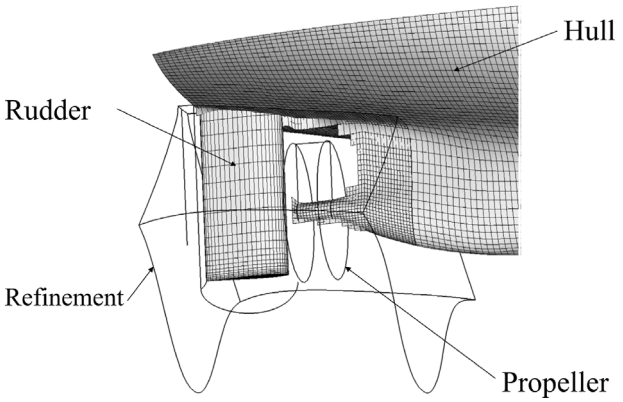

Fig. 5. Grids representing the aft part of the hull, including local refinement, along with the rudder and propeller.

The roughness is quantified using the equivalent sand grain roughness height, k_S .

XCHAP uses structured grids. A single block grid is typically generated for a bare hull case. A double-model approach is used where a symmetry condition is applied to the still-water plane, Fig. 4. Multi-block structured or overlapping grids are applied for more complex geometries such as hulls with appendages, and local grid refinements, Fig. 5.

To simulate the effect of the propeller, body forces are introduced. When the flow passes through the propeller swept volume, its linear and angular momentum increase as if it had passed a propeller with an infinite number of blades. The forces vary in space, but are independent of time, and generate a propeller-induced steady flow. The body forces are computed with a built-in lifting line propeller analysis program, Zhang (1990). Additionally, a friction resistance component is accounted for that contributes to the propeller torque. This simple modeling is also used to take into account the blade roughness.

The computation of the body forces is embedded in an iterative procedure, where first the current approximation of the velocity field is extracted at a representative propeller plane. The effective wake is thereafter obtained by subtracting the induced propeller wake. This is the function of the propeller code and is computed by the circulation from the previous iteration in the lifting line method. The new circulation and forces are computed in the effective wake. Thereafter, the forces are distributed over the volume cells in the cylindrical grid. The body forces are added to the right-hand side of the flow equations. This will give a new velocity field after solving the equations. The body forces are updated in every iteration. At convergence, the total wake computed by the RANS solver and the lifting line method should match in the selected propeller plane.

To simulate self-propulsion, the program automatically adjusts the propeller rotational speed to achieve a balance between resistance and thrust, ITTC (2017a).

The momentum and continuity equations are coupled, while the turbulent quantities are solved separately. A Krylov-type solver from the PETSc software suite, PETSc (2020a), is used to solve linear equations. The selected GMRES, PETSc (2020b), with the block Jacobi preconditioner, PETSc (2020c), is in this case very efficient, both in terms of convergence speed and stability.

3. Case description

A Korean VLCC test case (KVLCC2) developed by Korea Research Institute of Ships and Ocean Engineering, KRISO (formerly MOERI), was selected for this investigation. The ship and the propeller particulars are found in Table 1 and Table 2. Many experimental facilities have tested the model. In this paper, we will use recent data from SSPA, Sweden. The measurements include resistance, propulsion in scale 1:45.7 and seakeeping properties of the hull in scale 1:68.

Table 1
KVLCC2 main particulars.

Length between perpendiculars	L_{PP}	m	320.0
Length of waterline	L_{WL}	m	325.5
Maximum beam of waterline	B_{WL}	m	58.0
Draft	T	m	20.8
Displacement volume	∇	m^3	312 622
Wetted surface area	S	m^2	27 194
Block coefficient	C_B	–	0.8098
Midship section coefficient	C_M	–	0.9980
Longitudinal centre of gravity	$\overline{LCG}$	m	171.1
Vertical centre of gravity	$\overline{KG}$	m	18.6
Roll radius of gyration	kxx	m	23.2
Pitch radius of gyration	kyy	m	80.0
Frontal area	AF	m^2	1 200

Table 2
KP458 propeller particulars.

Type	–	–	Fixed Pitch
No. of blades	Z	–	4
Diameter	D	m	9.86
Pitch/Diameter ratio	$P/D(0.7R)$	–	0.721
Expanded area ratio	A_E/A_0	–	0.431
Hub ratio	d_h/D	–	0.155

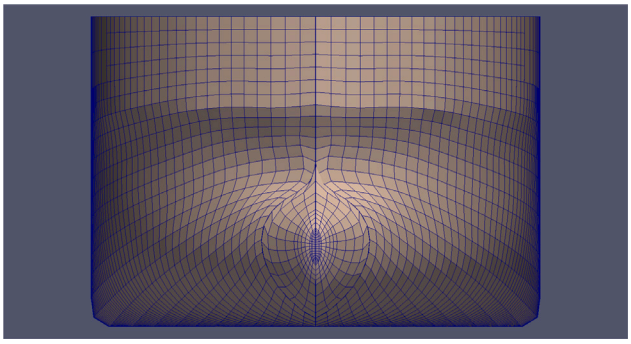

Fig. 6. Bow view of hull mesh with approximately 7000 panels.

4. Computational setup

4.1. Added resistance in waves

The hull panelization from the internal mesh engine can be seen in Figs. 6 and 7. The panelization is based on a block-structured mesh and has automatically been refined around the bow, stern, and waterline as well as in regions with large curvature. This is the coarse mesh in the grid refinement study.

The hull panels cover the entire hull, but in the computation, only the panels, entirely or partially, below the free surface are being used by the solver in each time step.

In Fig. 8 the initial free surface mesh is shown. The domain extends $4L_{PP}$ in all directions from the centre of the hull, and the free surface Cartesian background mesh has 24 panels in each direction. These panels are refined 6 times close to the hull, see Fig. 9.

The hull has no appendages in the SHIPFLOW MOTIONS setup. It starts from rest and is accelerated up to full speed. When the nominal speed is achieved the hull is released and towed with a spring preloaded to balance the friction resistance. The computations are set to simulate 20 s in model scale resulting in 46 wave encounters for the shortest and 9 wave encounters for the longest waves, respectively.

For the simulations in waves, the free surface is initialized with the undisturbed incident wave field and for the simulations in calm water, the fluid is initialized to be completely calm. As the computation progresses and the hull accelerates, the free surface disturbance from the hull grows, and panels further away from the hull are refined based on panel size and how large the free surface disturbance is. The added resistance is obtained by subtracting the resistance in calm water from the resistance in waves, both computed with MOTIONS.

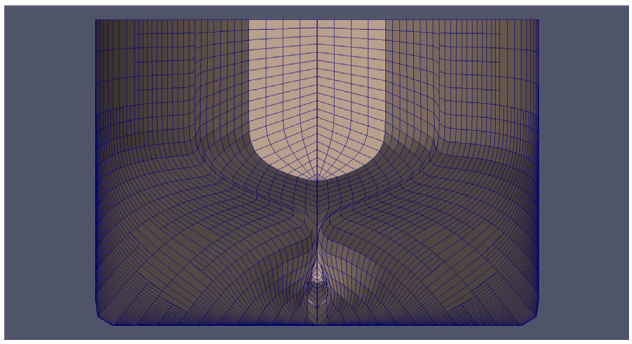

Fig. 7. Stern view of hull mesh with approximately 7000 panels.

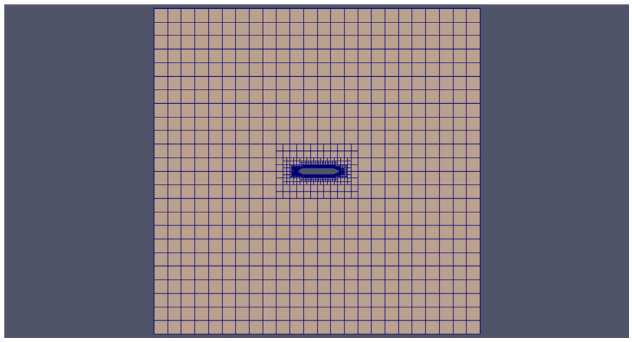

Fig. 8. The initial free surface panelization.

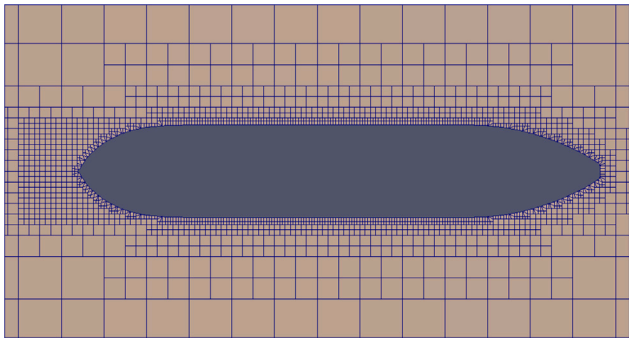

Fig. 9. Zoomed in view of the initial free surface panelization.

The incident regular waves are modeled with the 5th-order Stokes wave theory.

Settings for the meshes and the time step size are kept the same for the whole set of computations to avoid scatter in the results due to discretization as much as possible.

4.2. Calm water resistance and delivered power

To compute the wave pattern, dynamic sinkage, and trim, the XPAN module, which employs the nonlinear potential flow method, is utilized. A wave-cut integration method is employed for evaluating the wave resistance. Computing the viscous pressure resistance and friction involves using the RANS method XCHAP. For the RANS computations, an H-O structured background grid describing the hull is complemented with overlapping component grids. The domain extends 0.8 L_{PP} in front of and behind the hull, and the outer radius of the semi-cylindrical

Table 3
Cell sizes in selected regions, non-dimensionalized with L_{PP}.

GRID	Length-wise		Girth-wise	y^+
	forebody	aftbody	midship	midship
1	0.58× 10^{-3}	0.41× 10^{-3}	1.50× 10^{-3}	0.495
6	1.38× 10^{-3}	0.97× 10^{-3}	3.57× 10^{-3}	1.177

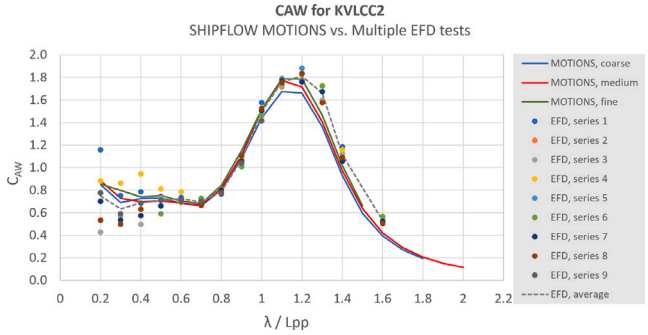

Fig. 10. Coefficient of added resistance due to regular, head sea waves for multiple measurements and simulations with three grid densities.

domain is 3.0 L_{PP}. Behind the submerged part of the transom, a separate grid block is used. An additional cylindrical domain represents the propeller. The separate rudder grid is of O-O type. The propeller and the rudder are encapsulated within a local refinement that is based on the background grid, where each cell is split to generate eight new cells. A detailed description of the applied boundary conditions is given in Broberg et al. (2022).

The simulations are performed with the fluid properties corresponding to the towing tank test conditions at model scale, and 15 °C seawater at full scale. The average hull roughness at full scale is assumed to be 100 μm.

4.3. Delivered power in waves

To obtain the delivered power in waves, two additional resistance components are introduced to the self-propulsion simulations. The first is the added resistance in waves, which was detailed in Section 4.1. The second resistance component taken into account is wind resistance. For this, we utilize the empirical method proposed by Fujiwara et al. (2005). These resistance values act as opposing forces, or 'negative towing forces', within the XCHAP solver.

5. Comparison of simulations with experimental results

5.1. Added resistance in regular waves

With the current potential flow method which uses an adaptive grid technique and employs breaking wave suppression mechanisms, see Kjellberg et al. (2022), it is not feasible to perform a strict verification study. The typical behavior of a free surface potential flow method in a systematic mesh refinement study would end up with a grid density where wave-breaking starts to appear, leading to divergence of the solution. Furthermore, the wave breaking suppression modeling employed in the current method begins to deteriorate at such small scales. In the current framework, the mesh is automatically refined to capture the free surface waves more accurately, but at the same time, the overall wave steepness is limited, and wave overturning is prevented. Therefore, a basic study is presented with three mesh resolutions to illustrate the general response to mesh refinement. The computed added resistance in regular waves at 15.5 knots of speed corresponding to Froude number Fr=0.142, is plotted in Fig. 10 together with the available test data. The measurements were performed at the

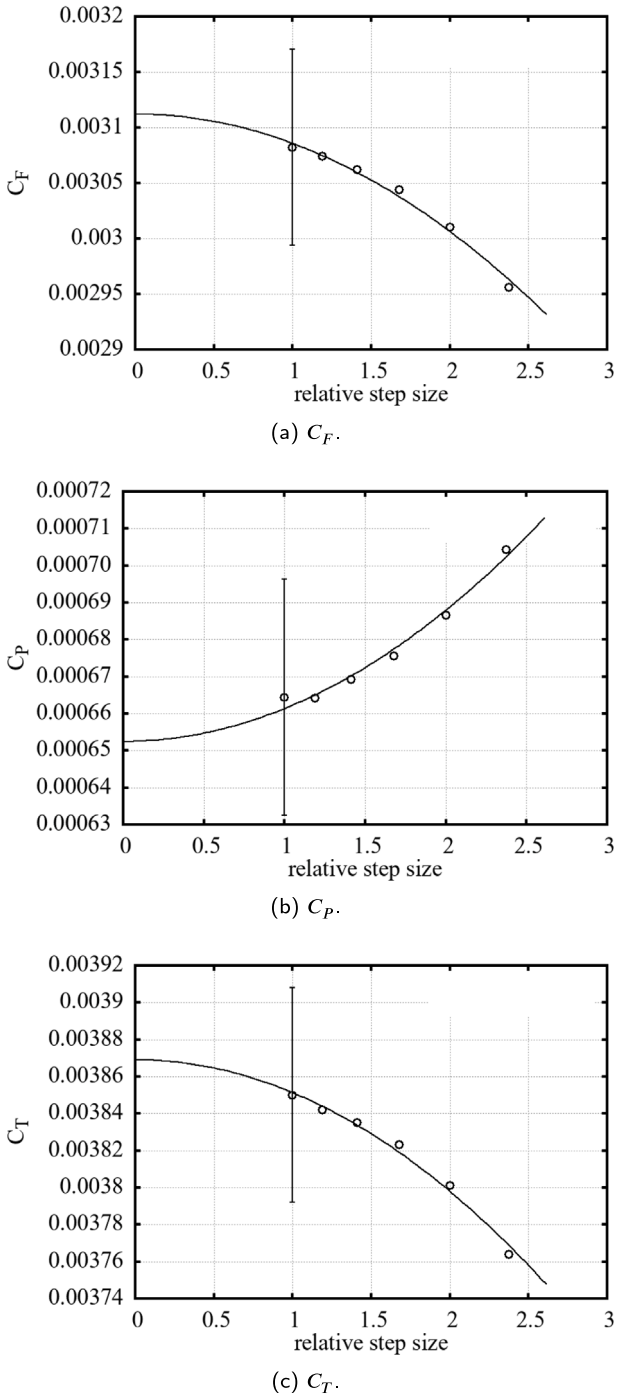

Fig. 11. Grid convergence of frictional, viscous pressure and total resistance coefficients, resistance at model scale. Error bar indicates uncertainty for the finest grid.

Maritime Dynamics Laboratory of SSPA. The collection includes multiple test series for all wave lengths, including tests with a self-propelled model and tests where the model is towed with soft springs, which is extremely valuable and not often presented, see Kjellberg and Gerhardt (2019) for further details. Even though there is a significant scatter in the data, especially for the shortest wave lengths, the simulations can be compared to the average value to judge the accuracy of the numerical method.

The simulation results are within the scatter found in the measurements for all three grid densities for λ/Lpp between 0.2 to 1.0, which is

Table 4
Total resistance coefficient uncertainty and deviations from the infinitely large grid.

GRID	$n_g \times 10^6$	$C_T \times 10^{-3}$	$U_G \% S_i$	$\lvert C_{Ti} - C_{T0} \rvert \% C_{T0}$
0	∞	3.869	–	–
1	16.6	3.850	1.5%	0.5%
2	9.9	3.842	2.1%	0.7%
3	5.9	3.835	2.9%	0.9%
4	3.5	3.823	4.1%	1.2%
5	2.1	3.801	5.8%	1.8%
6	1.2	3.764	8.2%	2.7%

essential to the current investigation. The longest waves do not overlap with the irregular wave energy spectrum of the investigated sea state, which will be seen later.

From the presented validation, it can be concluded that the viscous effects on added resistance in waves are limited for these conditions. In fact, the measurement accuracy should be of greater concern, especially for shorter waves. For the following resistance computations in this paper, the coarse mesh was used to minimize the computational time.

5.2. Calm water resistance and delivered power

The verification is carried out to investigate the numerical uncertainty. It is performed for a resistance case at the design speed. The least square root, LSR, is the method used to determine the numerical uncertainty and the order of accuracy, Eça and Hoekstra (2014). A software tool prepared by MARIN, MARIN (2018), is used to process the results.

The grid refinement ratio is $\sqrt[4]{2}$ in each direction of the structured volume grid for RANS simulations. The total number of cells ranges from 1.2×10^6 to 16.6×10^6 at model scale. The cell sizes in selected regions for the finest (#1) and coarsest (#6) grids are given in Table 3. The length and girth-wise sizes are non-dimensionalized by L_{PP}. It should be noted that the aftbody cell size in the length-wise direction is given in a region where the overlapping grid refinement is used. The number of cells in the normal direction for the full-scale simulations is about 65% larger compared to the model scale, to compensate for the clustering of cells close to the hull, due to the stretching necessary to keep y^+ according to the requirements of the turbulence model.

The grid convergence results are plotted in Fig. 11. The horizontal axis represents the relative step size between the grids. The total resistance coefficient and its frictional and pressure components indicate monotonous grid convergence with small uncertainties and limited scatter.

Table 4 contains C_T results obtained for all grid sizes, n_g, as well as the value extrapolated to an infinite number of cells. Since it is often not practical to use the finest grid that was included in the verification study, the uncertainties for coarser grids are also very important, here expressed as a percentage of the solution for each grid, S_i. The last column can be of particular interest to the designers. It shows a difference between C_{T0}, the value extrapolated to zero step size, and each grid result, C_{Ti}, in percent of C_{T0}.

Considering the computational effort, the fourth-finest grid from the verification step is used in the validation. To validate the computed results, the computations are compared to the model-scale towing tank measurements of the total resistance, Fig. 12. The total resistance average comparison error is about 1% for all three speeds that are considered. The delivered power computations in full-scale are compared to the measurements extrapolated to full-scale with the ITTC78 method, Fig. 13. The average comparison error is about 1% for all three speeds. The roughness effects on the hull and propeller at full scale are computed using the model implemented in the RANS code, while the aerodynamic resistance is added using the ship's frontal area and a coefficient provided by the model testing facility. Since there are no sea trials available for KVLCC2, only the comparison with the extrapolated model tests is possible. However, a full-scale validation of a smaller tanker for the same numerical method has been published earlier, Orych et al. (2021)

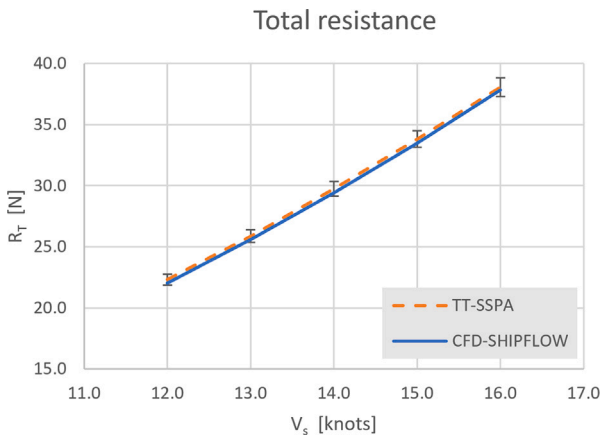

Fig. 12. Validation of total resistance measured at SSPA towing tank and CFD simulations. Error bars indicate 2% error for reference.

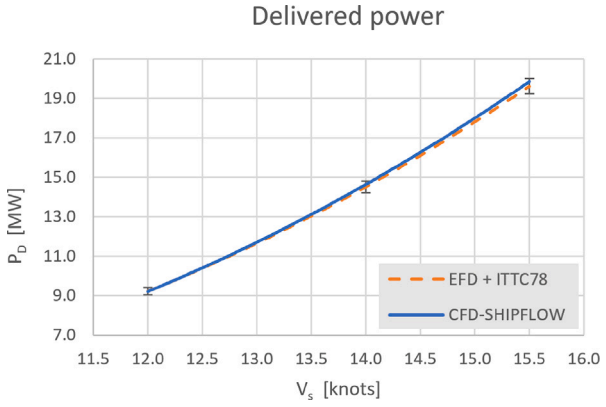

Fig. 13. Comparison of full-scale delivered power extrapolated from measurements with ITTC78 method and predicted by CFD simulations. Error bars indicate 2% error for reference.

6. Speed loss prediction

The speed loss of a ship in a seaway can be expressed as a weather factor, f_w, calculated from the speed achieved in certain wave and wind conditions and the speed in calm water at the same delivered power. In the ITTC guidelines, ITTC (2021b), three methods are illustrated: experiments, numerical simulations or empirical formulas can be used to achieve various levels of fidelity. The high-fidelity methods are often less practical due to the cost and time involved. The method presented here can be used in the ship design stage but at the same time give good accuracy, see Fig. 14 where the current approach is highlighted.

6.1. Added resistance in waves

The added resistance in waves is computed for three speeds, 12.5, 13.5 and 14.5 knots (Froude number of 0.11, 0.12 and 0.13) and three wave directions, 0° (head waves), 30° and 60°, for a range of regular wave lengths from 0.2 to 1.8 λ/L_{PP}, see Fig. 15 illustrating the C_{AW} at 14.5 knots of ship speed. The response in the shortest waves, below $\lambda/L_{PP} = 0.2$, is estimated with STAwave-II method, ITTC (2021a). It is an empirical method developed to estimate the transfer function related to the average increase in resistance for a ship in regular head waves. This method uses primary parameters such as the dimensions of the ship and its speed. To achieve this, a comprehensive array of seakeeping model test results for a large number of ships has been utilized. The STAwave-II method addresses both types of resistance

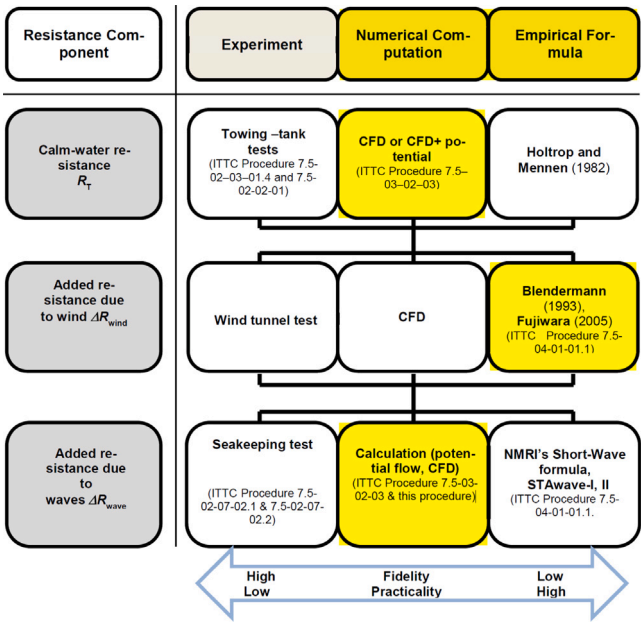

Fig. 14. Methods used to determine total resistance in waves, ITTC (2021b).

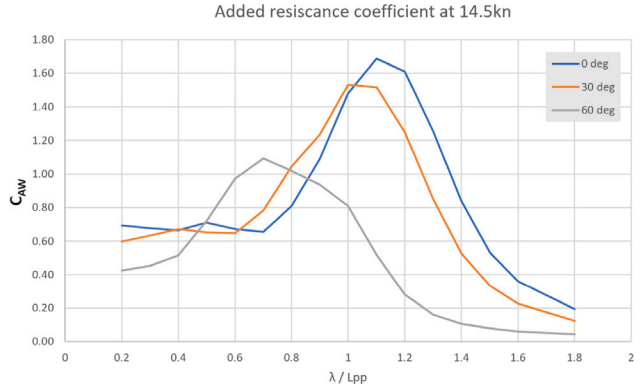

Fig. 15. C_{AW} for three wave directions at 14.5 knots, Fr=0.13.

increase in wave conditions: the wave reflection-induced increase and the motion-induced resistance.

The mean resistance in irregular waves is calculated by integrating the transfer function of the mean added resistance in regular waves with the wave spectrum, $S(\omega)$. The mean resistance increase for irregular waves is given by

$$\overline{R_{AW}(\alpha)} = 2\int_0^{2\pi} \frac{R_{\mathrm{AW}}(\omega,\alpha)}{\zeta_A^2(\omega)} S(\omega)\, d\omega \tag{1}$$

where $R_{\mathrm{AW}}(\alpha)$ is the mean resistance increase in regular waves for a given wave direction, and ζ_A is the corresponding wave amplitude.

For the weather factor calculations, a spectrum described in ITTC with significant wave height, H_S, of 3.0 m and zero up-crossing period, T_Z, of 6.16 s is used. The wave spectrum given by IMO (2012) is:

$$S = \frac{A_S}{\omega^5} e^{-\frac{B_S}{\omega^4}} \tag{2}$$

where

$$A_S = \frac{H_S^2}{4\pi}\left(\frac{2\pi}{T_Z}\right)^4 \text{ and } B_S = \frac{1}{\pi}\left(\frac{2\pi}{T_Z}\right)^4 \tag{3}$$

When the spectrum and C_{AW} are plotted together it can be seen that for this sea state, the wave energy is concentrated in the region between

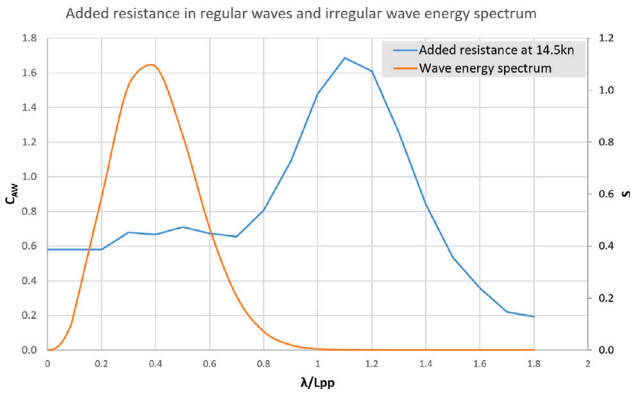

Fig. 16. Irregular wave energy spectrum and ship added resistance coefficient in regular head waves at 14.5 knots.

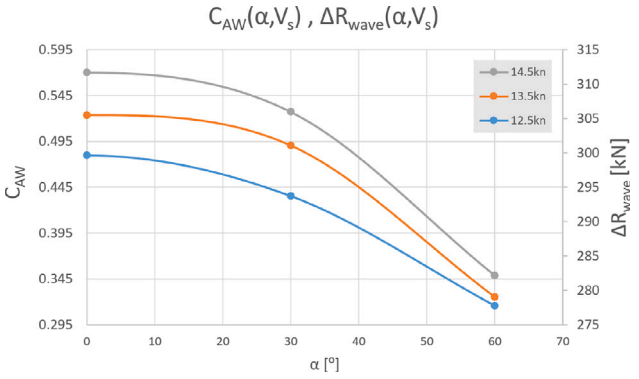

Fig. 17. Mean added wave resistance for three speeds as a function of wave direction.

0.1 to 0.8 λ/L_{PP}, while the C_{AW} peak is outside of these conditions, see Fig. 16. Therefore, the mean added resistance due to the waves will depend more on the wave reflection and diffraction rather than radiation, i.e. the motion-induced resistance.

The mean added wave resistance for the KVLCC2 hull for three speeds for three different wave directions is illustrated in Fig. 17. The maximum values for each speed occur for the head waves.

An additional simulation is carried out in irregular waves at the highest speed in head waves. This is done to check if the results would be similar to those obtained by integrating the regular wave transfer function of the mean resistance with the irregular wave energy spectrum. Sea state 5 wave spectrum according to ITTC, is realized with a significant wave height of 3.0 m and a zero up-crossing period of 6.16 s. The wave energy spectrum is shown in Fig. 16. Using the same mesh as in the regular waves, the simulations are executed for 320 seconds in full-scale, corresponding to 110 wave encounters, zero up-crossings, in this case. The longer simulation is needed to provide sufficient statistical data for obtaining the average resistance. The difference between integrating the added resistance in regular waves with the wave spectrum and the added resistance computed in irregular waves is about 5%. This test is done to cross-check the numerical results and see if the simulation time can be shortened. In this case, running in irregular waves takes about half the time needed for the entire range of regular waves. The authors do not have the measurements in the irregular waves for this particular case to illustrate the validity, but the simulation results seem promising both in terms of agreement with the regular waves and the execution time.

6.2. Speed-power curves

The weather factor, f_w signifies the percentage of the ship's calm water speed that it can sustain when encountering Beaufort 6 weather

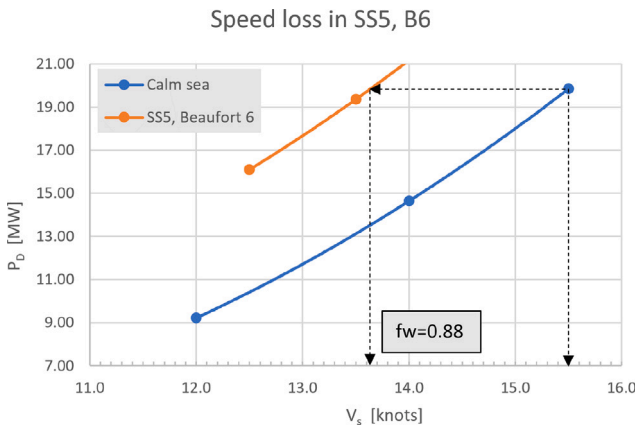

Fig. 18. Speed-power curves for calm water and in State 5 head seas with Beaufort 6 wind.

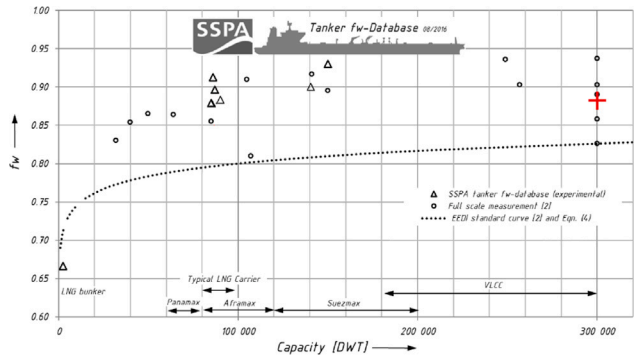

Fig. 19. f_w database for tankers, Gerhardt and Kjellberg (2017). The result from the current method is marked with red "+" symbol.

conditions and corresponding waves, Gerhardt and Kjellberg (2017). Estimating that factor requires power prediction in calm water and in waves. The resistance due to the waves and the apparent wind is added as an external force in the self-propulsion simulations. For both conditions, we compute the delivered power, and the speed loss at the given P_D is estimated, see Fig. 18. In this case, the weather factor is 0.88. It is about 6.5% higher than the more conservative standard curve for the weather factor in EEDI, which represents the effect of wind and waves on the energy efficiency of a ship (IMO, 2012). The simulation result corresponds well also to the excerpt from SSPA's database for tankers, see Fig. 19.

7. Discussion

The presented method attempts to deliver accurate and fast predictions of power requirements for ships sailing in waves. It combines the unsteady potential flow simulations in waves with the steady state self-propulsion at full scale. On average, the simulations require approximately 1.5 h per case in waves and 2 h for self-propelled cases on a single node with a 24-core CPU. Assuming that a sufficient number of runs are completed, such as 8 wave lengths for the seakeeping part and 6 propelled cases to estimate delivered power, the total time required for assessing the speed loss is approximately one day.

Since the mean added resistance in waves and the aerodynamic resistance are directly used in the propulsion simulations to increase the total resistance, this approach certainly has its limitations. The propeller performance is not affected by the time-varying wake, propeller and free surface interactions, submergence and loading. This technique is compared with quasi-steady and fully unsteady approaches in Saettone et al. (2020). The described relative propeller torque difference between steady and unsteady approach for wave length $\lambda/L = 1.0$ with 2% steepness, is about 2.5% and diminishes with lower wave heights and shorter lengths. For the case presented in the current paper, the sea state 5 spectrum peak is at $\lambda/L = 0.4$ and the energy spectrum goes to zero at $\lambda/L = 1.0$. The pitch and heave responses are small, and the propeller submergence is not changed significantly. It is likely that the time-varying flow effects are small for the presented case, but further investigation is necessary to confirm this assumption.

By analyzing its limitations, we can determine the range of applications for which this method can be confidently used. However, it should be noted that spray, large hull motions that may result in propeller ventilation, or high propeller loading cannot be precisely accounted for. Nevertheless, the presented method shows reliable predictions for standard seakeeping tests conducted in regular waves. Furthermore, the simulations conducted in irregular waves for a moderate sea state show good agreement with the integrated irregular wave spectrum and transfer function of the mean added resistance observed in regular waves. These results suggest that the presented approach could serve as a valuable complement to physical testing, offering ship designers a useful tool for initial design and optimization.

8. Conclusions

The main objective of this paper is to present an efficient and accurate numerical method to estimate the power requirements in waves. The method is suitable for calculations of the added power in waves or the weather factor, f_w, of the attained energy efficiency design index for new ships, EEDI. The comparison between the numerical simulations and the experimental results of the resistance, the delivered power and the added resistance in waves indicate good accuracy. The resistance and the delivered power comparison errors are about 1% at the considered speeds. The estimated weather factor is consistent with the values derived from full-scale measurements included in the example database of similar ships. However, the accuracy may deteriorate for relatively larger waves where the time-varying wake, propeller submergence and loading cannot be neglected.

CRediT authorship contribution statement

Michal Orych: Conceptualization, Methodology, Software, Validation, Visualization, Writing – original draft. **Magnus Östberg:** Methodology, Software, Validation, Writing – original draft. **Martin Kjellberg:** Methodology, Software, Validation, Writing – original draft. **Sofia Werner:** Data Curation, Writing – review & editing. **Lars Larsson:** Supervision, Writing – review & editing.

Declaration of competing interest

The authors declare that they have no known competing financial interests or personal relationships that could have appeared to influence the work reported in this paper.

Data availability

Data will be made available on request.

Acknowledgments

The authors would like to thank: Energimyndigheten, Sweden (Swedish Energy Agency, project 49300-1) for the financial support and SSPA AB for providing highly valuable validation data.

References

Barnes, J.E., Hut, P., 1986. A hierarchical O(n-log-n) force calculation algorithm. Nature 324, 446.

Broberg, L., Regnström, B., Östberg, M., 2022. XCHAP – Theoretical Manual. FLOWTECH International AB, Gothenburg, Sweden.

Chakravarthy, S., Osher, S., 1985. A new class of high accuracy TVD schemes for hyperbolic conservation laws. In: 23rd Aerospace Sciences Meeting, Reno, NV, U.S.A., AIAA Paper No 85–0363.

Coslovich, F., Kjellberg, M., Östberg, M., Janson, C.-E., 2021. Added resistance, heave and pitch for the KVLCC2 tanker using a fully nonlinear unsteady potential flow boundary element method. Ocean Eng. 229, 108935. http://dx.doi.org/10.1016/j.oceaneng.2021.108935, URL: https://www.sciencedirect.com/science/article/pii/S002980182100370X.

Deng, G.B., Queutey, P., Visonneau, M., 2005. Three-dimensional flow computation with Reynolds Stress and Algebraic Stress Models. In: Procedings of the ERCOFTAC International Symposium on Engineering Turbulence Modelling and Measurements; ETMM6, Sardinia, Italy, 23–25 May, 2005. pp. 389–398.

Dick, E., Linden, J., 1992. A multigrid method for steady incompressible Navier-Stokes equations based on flux difference splitting. Internat. J. Numer. Methods Fluids 14, 1311–1323.

Duchon, J., 1976. Splines minimizing rotation-invariant semi-norms in Sobolev spaces. In: Schempp, W., Zeller, K. (Eds.), Constructive Theory of Functions of Several Variables: Proceedings of a Conference Held at Oberwolfach, Germany, April 25 - May 1, 1976. In: Lecture Notes in Mathematics, vol. 571, Springer, pp. 85–100.

Ducrozet, G., Engsig-Karup, A.P., Bingham, H.B., Ferrant, P., 2014. A non-linear wave decomposition model for efficient wave-structure interaction. Part A: Formulation, validation and analysis. J. Comput. Phys. 257, 863–883.

Eça, L., Hoekstra, M., 2014. A procedure for the estimation of the numerical uncertainty of CFD calculations based on grid refinement studies. J. Comput. Phys. 262, 104–130.

Fujiwara, T., Ueno, M., Ikeda, Y., 2005. A new estimation method of wind forces and moments acting on ships on the basis of physical component models. J. JASNAOE 2.

Gerhardt, F.C., Kjellberg, M., 2017. Determining the EEDI 'Weather Factor' FW. In: Influence of EEDI on Ship Design & Operation, 13 September 2017, London.

Hino, T., Stern, F., Larsson, L., Visonneau, M., Hirata, N., Kim, J., 2021. Numerical ship hydrodynamics. In: An Assessment of the Tokyo 2015 Workshop. In: Lecture Notes in Applied and Computational Mechanics, vol. 94, Springer Nature, Switzerland, http://dx.doi.org/10.1007/978-3-030-47572-7.

IMO, 2012. Interim Guidelines for the Calculation of the Coefficient FW for Decrease in Ship Speed in a Representative Sea Condition for Trial Use. IMO Circular MEPC.1/Circ.796.

IMO, 2018. Guidelines on the Method of Calculation of the Attained Energy Efficiency Design Index (EEDI) for New Ships. RESOLUTION MEPC.308(73).

IMO, 2022. Guidelines on the Method of Calculation of the Attained Energy Efficiency Existing Ship Index (EEXI). Resolution MEPC.350(78).

ITTC, 2017a. 1978 ITTC Performance Prediction Method, ITTC Quality System Manual, Recommended Procedures and Guidelines. Propulsion Committee of the 28th ITTC.

ITTC, 2021a. Preparation, Conduct and Analysis of Speed/Power Trials, ITTC Quality System Manual, Recommended Procedures and Guidelines. Specialist Committee on Ships in Operation at Sea of the 29th ITTC.

ITTC, 2021b. Calculation of the Weather Factor f_w for Decrease of Ship Speed in Wind and Waves, ITTC Quality System Manual, Recommended Procedures and Guidelines. Specialist Committee on Ships in Operation at Sea of the 29th ITTC.

Janson, C.-E., 1997. Potential Flow Panel Methods for the Calculation of Free-Surface Flows with Lift (Ph.D. thesis). Chalmers University of Technology, Gothenburg, Sweden.

JoRes, 2023. JoRes Web Page. https://jores.net.

Kim, M., Hizir, O., Turan, O., Day, S., Incecik, A., 2017. Estimation of added resistance and ship speed loss in a seaway. Ocean Eng. 141, 465–476. http://dx.doi.org/10.1016/j.oceaneng.2017.06.051.

Kjellberg, M., Gerhardt, F.C., 2019. Improved methods for the experimetal determination of "added resistance in waves". In: AMT Conference <9-11 October 2019, Rome Italy.

Kjellberg, M., Gerhardt, F., Werner, S., 2022. Sailing in waves : A numerical method for analysis of seakeeping performance and dynamic behavior of a wind powered ship. In: SNAME 24th Chesapeake Sailing Yacht Symposium, CSYS 2022. Society of Naval Architects and Marine Engineers, RISE Research Institutes of Sweden, Maritime department.

Korkmaz, K.B., 2015. CFD Predictions of Resistance and Propulsion for the JAPAN Bulk Carrier (JBC) with and Without an Energy Saving Device (MSc Thesis). Chalmers University of Technology, Gothenburg, Sweden.

Larsson, L., Stern, F., Visonneau, M., 2014. Numerical Ship Hydrodynamics - An Assessment of the Gothenburg 2010 Workshop. Springer Verlag, http://dx.doi.org/10.1007/978-94-007-7189-5.

MARIN, 2018. Numerical Uncertainty Analysis – User Manual. MARIN, The Netherlands.

Mola, A., Heltai, L., DeSimone, A., 2017. Wet and dry transom stern treatment for unsteady and nonlinear potential flow model for naval hydrodynamics simulations. J. Ship Res. 61, 1–14.

Orych, M., Werner, S., Larsson, L., 2021. Validation of full-scale delivered power CFD simulations. Ocean Eng. 238, 109654. http://dx.doi.org/10.1016/j.oceaneng.2021.109654.

Orych, M., Werner, S., Larsson, L., 2022. Roughness effect modelling for wall resolved RANS – Comparison of methods. Ocean Eng. 266, 112778. http://dx.doi.org/10.1016/j.oceaneng.2022.112778.

PETSc, 2020a. PETSc web page. https://www.mcs.anl.gov/petsc/index.html.

PETSc, 2020b. PETSc documentation, solvers. https://www.mcs.anl.gov/petsc/petsc-current/docs/manualpages/KSP/KSPGMRES.html.

PETSc, 2020c. PETSc documentation, preconditioners. https://www.mcs.anl.gov/petsc/petsc-current/docs/manualpages/PC/PCBJACOBI.html.

Roe, P.L., 1981. Approximate Riemann solvers, parameter vectors, and difference schemes. J. Comput. Phys. 43, 357.

Saettone, S., 2020. Ship Propulsion Hydrodynamics in Waves (Ph.D. thesis). Technical University of Denmark.

Saettone, S., Tavakoli, S., Taskar, B., Jensen, M.V., Pedersen, E., Schramm, J., Steen, S., Andersen, P., 2020. The importance of the engine-propeller model accuracy on the performance prediction of a marine propulsion system in the presence of waves. Appl. Ocean Res. 103, 102320. http://dx.doi.org/10.1016/j.apor.2020.102320, URL: https://www.sciencedirect.com/science/article/pii/S0141118720302893.

Zhang, D.H., 1990. Numerical Computation of Ship Stern/Propeller Flow (Ph.D. thesis). Chalmers University of Technology, Gothenburg, Sweden.

Zhang, Y., Kim, B., 2018. A fully coupled computational fluid dynamics method for analysis of semi-submersible floating offshore wind turbines under wind-wave excitation conditions based on OC5 data. Appl. Sci. 8 (11), URL: https://www.mdpi.com/2076-3417/8/11/2314.